ELSEVIER

Contents lists available at ScienceDirect

Journal of Membrane Science

journal homepage: www.elsevier.com/locate/memsci





Stochastic microstructure delineation and flow simulation in asymmetric block copolymer ultrafiltration membranes

M. Sadegh Riasi ^{a,1}, Lieihn Tsaur ^{b,1}, Yuk Mun Li ^{b,c}, Qi Zhang ^b, Ulrich Wiesner ^{b,d}, Lilit Yeghiazarian ^{a,*}

- ^a Department of Chemical and Environmental Engineering, University of Cincinnati, Cincinnati, OH, 45221, USA
- ^b Department of Materials Science and Engineering, Cornell University, Ithaca, NY, 14853, USA
- ^c Robert Frederick Smith School of Chemical and Biomolecular Engineering, Cornell University, Ithaca, NY, 14853, USA
- ^d Kavli Institute at Cornell for Nanoscale Science, Cornell University, Ithaca, NY, 14853, USA

ARTICLEINFO

Keywords: Pore-scale flow modeling Permeability Hierarchical structures Ultrafiltration membrane Block copolymer

ABSTRACT

Asymmetric block copolymer ultrafiltration membranes have a wide range of applications from water purification and virus filtration all the way to drug delivery. Although optimizing flow is critical to the performance of such ultrafiltration membranes, their numerical flow characterization has remained challenging. The main problems include hierarchical pore structure delineation and lack of an efficient, image-based pore-scale modeling approach. In this study, we use 2D scanning electron microscopy (SEM) images with a variety of resolutions to delineate the hierarchical asymmetric pore structure. To simulate flow, a novel stochastic pore network model is proposed. The absolute permeabilities of two asymmetric block copolymer ultrafiltration membranes are computed and compared with experimental results showing good agreement.

1. Introduction

Ultrafiltration membranes have a wide range of applications ranging from water purification, protein separation, and virus filtration to drug delivery [1,2]. A class of ultrafiltration membranes that has received much attention in the past decade is asymmetric block copolymer (BCP) membranes synthesized *via* a hybrid block copolymer self-assembly and non-solvent induced phase separation process first introduced by Peinemann et al. [3], and later coined SNIPS [4].

A key advantage of SNIPS membranes is that their integral asymmetric structure eliminates the permeability-selectivity tradeoff. BCP self-assembly on the top surface gives rise to a thin (~100 nm), ordered, isoporous separation layer that ensures high permselectivity, whereas the hierarchical meso- to macroporous substructure provides mechanical stability. Pore sizes in the separation layer can be tailored to the desired application by varying the BCP molar mass or by incorporating additives into the casting dope [5,6]. Membrane substructure can be tuned from sponge-like to finger-like by systematically varying casting parameters such as polymer concentration and evaporation time [7]. Sponge-like substructures have densely packed pores and are typically

less permeable than finger-like substructures, which are characterized by macrovoids ("fingers") that extend from the bottom of the membrane up to the separation layer [8]. This study focuses on SNIPS membranes with sponge-like substructures.

Optimizing flow is critical to the performance of BCP ultrafiltration membranes, however, little has been reported on their numerical flow characterization [9,10]. One of the main challenges is the delineation of the hierarchical pore structure. Due to the wide pore size distribution throughout the SNIPS membrane substructure, acquiring a full high-resolution three-dimensional (3D) reconstruction is cumbersome and costly. For example, Sundaramoorthi et al. [11] had to use focused ion beam scanning electron microscopy (FIB/SEM) and serial block-face SEM (SBF/SEM) imaging techniques to create a 3D reconstruction of a BCP membrane, from which the porosity profile could be extracted. Most studies, however, simply restrict pore size characterization to the easily characterizable (e.g., via SEM) separation layer [12].

Another major challenge in flow characterization of BCP membranes is the lack of an image-based pore-scale modeling approach that is computationally efficient and that can capture such wide pore size distributions. Traditionally, analytical and empirical equations [13] are

E-mail address: yeghialt@ucmail.uc.edu (L. Yeghiazarian).

^{*} Corresponding author.

¹ Authors contributed equally.

used to study the effect of pore morphology on membrane permeability. Shi et al. [10] used GeoDict (Math2Market GmbH, Germany) to generate a 3D digital structure similar to that of asymmetric sponge-like and finger-like membranes and simulated flow using Stokes and Stokes—Brinkman equations. Although good agreement was achieved between computed and measured permeability, image segmentation techniques and SEM image data extraction were not described in the paper.

Pore-scale flow modeling approaches can generally be classified into topologically-consistent and stochastic. Topologically-consistent approaches are used when a 3D image of the porous medium is available. Examples range from direct numerical simulation (DNS) techniques, such as finite volume method (FVM) and lattice Boltzmann method (LBM), to computationally faster methods such as pore network modeling (PNM) and pore topology method (PTM) [14-16]. In the absence of a 3D image of the porous medium, stochastic approaches are used to investigate pore-scale flow properties. These methods are based on the statistical and empirical information available for the void space. One of the most widely used stochastic approaches is the stochastic version of the pore network modeling method, often referred to as stochastic pore network modeling (SPNM). SPNM uses statistical properties of the void space such as its pore size distribution, pore connectivity and pore density to create a network model of the porous structure, and employs simplified 1D equations or analytical relations to describe flow in each pore element. For an in-depth review of pore network modeling methods, readers are encouraged to read Xiong et al. [17].

In this study, we address the challenge of pore structure delineation by using an array of SEM images with different resolutions. Traditionally, the 3D information of BCP structures can be obtained using transmission electron microscopy (TEM) tomography, an approach that has recently been extended to substantially larger sample volumes via "sliceand-view" scanning electron microscopy (SVSEM, also known as FIB/ SEM) [18]. Such techniques are still limited, however, in both their accessibility as well as their sample volume relative to the dimensions of asymmetric ultrafiltration membranes described here. In contrast, regular SEM imaging equipment is readily available in electron microscopy imaging facilities world-wide, and was therefore used to provide imaging input for our studies. SEM images were segmented using a continuous max-flow and min-cut algorithm and collectively used to describe the pore size distribution and pore density profile of the membrane. To get insight into the 3D pore structure of the membrane, a 3D polymeric scaffold with larger pore structure is used. To address the challenge of pore-scale flow simulation, a novel stochastic pore network model is proposed and used to compute the absolute permeabilities of two block copolymer membranes, which are compared with experimental measurements.

The outline of this article is as follows. A brief overview of SNIPS membrane fabrication, imaging and permeability measurements is provided in Sections 2.1-2.3. Next, the structural properties of the membranes are discussed (Section 2.4) followed by detailed description of stochastic pore network generation and permeability calculation using SPNM (Section 2.5). In Section 2.6, a hypothesis is proposed on the structure of mesoporous walls that enables us to differentiate macropores from mesopores. This hypothesis is later used to delineate the hierarchical pore size distribution of the membrane. In Results (Section 3), we use the SEM images of an actual membrane to showcase the step-by-step process from raw SEM images to permeability calculations. Finally, the discussion of the results and conclusions are presented in Sections 4 and 5. Appendices (Appendix A-Appendix C) provide supplementary materials for a second membrane, the segmentation method and 3D feature extraction from the polymeric scaffold.

2. Materials and methods

2.1. Polymer synthesis and membrane fabrication

Two poly(isoprene-b-styrene-b-4-vinylpyridine) (ISV) triblock

terpolymers were synthesized using an established sequential anionic polymerization technique detailed elsewhere [19]. BCP characteristics were determined using a combination of tetrahydrofuran (THF) gel permeation chromatography (GPC) and ¹H nuclear magnetic resonance (NMR) in chloroform-d. ISV87 had a molar mass of 87 kg mol⁻¹, and poly(isoprene) (PI), poly(styrene) (PS) and poly(4-vinylpyridine) (P4VP) fractions of 28, 57, and 15 wt%, respectively. ISV138 had a molar mass of 138 kg mol⁻¹, and consisted of 20 wt% PI, 67 wt% PS, and 13 wt% P4VP. The polydispersity indices (PDI) of ISV87 and ISV138 were 1.14 and 1.18, respectively.

BCP membranes were fabricated using the SNIPS process [19]. Casting solutions were prepared by dissolving 11 wt% ISV87 (or ISV138) polymer in a binary solvent system of 1,4-dioxane (DOX) and THF (7:3 by weight) and stirring until homogeneous. Solutions were casted onto a glass substrate using an automated blade-casting system adjusted to a gate height between 0.203 mm and 0.229 mm. Films were allowed to evaporate for 80 s to drive self-assembly on the top surface and create a concentration gradient across the film depth. Thereafter, films were immersed in a non-solvent deionized (DI) water bath (18.2 $\mbox{M}\Omega\text{-cm}$) to precipitate out the membrane and kinetically trap the asymmetric pore structure stemming from the concentration gradient. Membranes were stored in DI water until further use.

2.2. Scanning electron microscopy

SEM images were acquired using either a Tescan Mira3 field emission scanning electron microscope (FE-SEM) equipped with an in-lens detector (accelerating voltage of 5 kV) or a Zeiss Gemini 500 SEM (accelerating voltage of 1.5 kV). Prior to imaging, all samples were coated with gold-palladium using a Denton Vacuum Desk II sputter coater. Images of the membrane top surface were used to delineate the ordered pore structure of the separation layer (Fig. 4c and Fig. A.1c). Sample cross-sections—used to analyze the pore size gradient of the membrane substructure—were prepared cryogenically. Cross-sectional micrographs of ISV87 and ISV138 at various magnifications are shown in Fig. 4a and Fig. A.1a, respectively.

2.3. Hydraulic permeability tests

Permeability tests were conducted using a 10 mL dead-end stirred cell (Amicon 8010, Millipore Co.) with an active area of 4.1 cm². The stirred cell was pressurized to 1 psi (0.07 bar) using N_2 gas, and the mass of permeated DI water was recorded using a balance. Hydraulic permeability of each membrane was reported as the ratio of volumetric filtrate flux ($Lm^{-2}h^{-1}$, LMH) to trans-membrane pressure (bar). The experimentally calculated hydraulic permeabilities were $484\pm66\,LMH/bar$ and $644\pm15\,LMH/bar$ for ISV87 and ISV138, respectively. Reported values are averages and standard deviations from three replicate measurements.

2.4. Membrane structure

ISV SNIPS membranes consist of a ~ 100 nm top separation layer integrated with a hierarchical meso- to macroporous substructure (Fig. 1a). The self-assembled top separation layer exhibits narrowly-dispersed mesopores forming a two-dimensional (2D) square lattice (Fig. 1c). A cross-sectional view of the separation layer shows the interconnected pore network characteristic of cubically packed micelles (Fig. 1b). The pores constituting the substructure increase in size as distance from the separation layer increases. As pore size increases, the walls themselves become mesoporous (Fig. 1d). Going forward, we will refer to the main pores in the substructure as *macropores* and the pores lining the walls as *mesopores*.

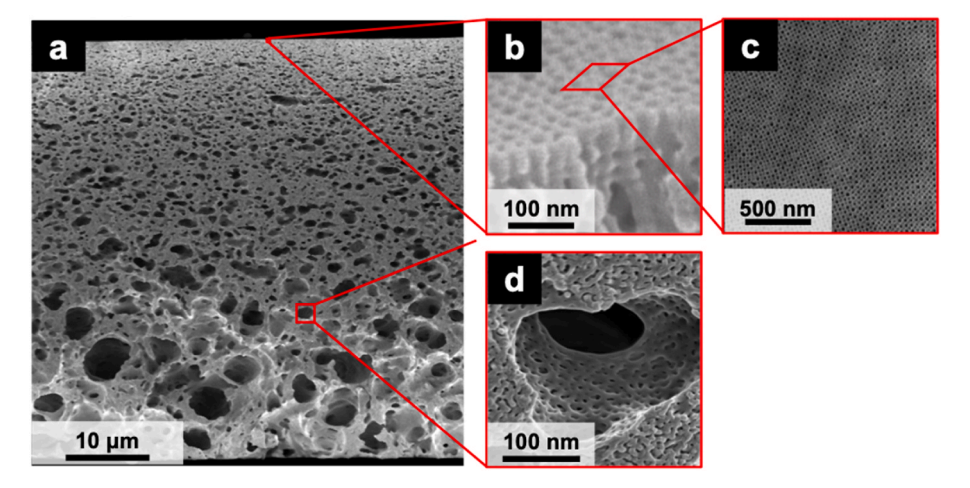


Fig. 1. Structure of sponge-like SNIPS membrane. (a) Membrane cross-section. (b) Cross-sectional view of the membrane top separation layer showing the interconnected pore network. This image is reproduced from Ref. [19]. (c) Top-view of the membrane separation layer. (d) Mesopores lining the walls of macropores. Note that the regions of interest shown with red rectangles/parallelograms do not necessarily represent the correct scale.

2.5. Stochastic pore network model (SPNM)

A pore network consists of pore bodies, representing the large pores in the structure, and pore throats, representing the flow path between each pair of pore bodies. The number of pore throats emanating from each pore body is called coordination number of the pore body. For instance, in the example network of Fig. 2c, the filled spheres represent the pore bodies and solid lines represent the pore throats. From a graph theoretical standpoint, a pore network can be viewed as an undirected graph where nodes represent pore bodies, links represent pore throats, and the coordination number represents the node degree.

In this study, we use a stochastic pore network modeling approach to compute membrane permeability. Such pore networks are generated solely based on the stochastic information available for the structure of the porous medium. We use pore density profile and coordination number distribution to generate a stochastic pore network. Pore density is defined as the number of pores per unit area. Since the membrane has an asymmetric structure, averaged structural properties are assumed to only vary in the direction perpendicular to the membrane surface (*i.e.*, the z-direction).

Due to the abrupt structural changes at the separation layer-

substructure interface, two separate pore networks will be generated. The resulting networks will be assembled using interface links [20], collectively representing the membrane microstructure. Once a representative pore network of the membrane is generated, a length and a pore throat diameter are assigned to each pore throat to compute permeability.

2.5.1. Pore network generation

The stochastic pore network model developed in this study builds upon the multi-directional pore network model [21] by introducing a pore density gradient. Our proposed algorithm requires three input parameters: dimensions of the network, pore density as a function of depth *z* and coordination number distribution.

First, we need to generate the skeleton of our network comprising cubic cells that will later contain the pore bodies. Following Fig. 2a, let w_n be the width of a cubic cell in layer n, where n=1,2,3,...,N, and z_n be the z-coordinate of the cubic cell centroid. As depicted in this figure, z_n can be related to the cell width through $z_n=(\sum_{i=1}^{n-1}w_i)+\frac{w_n}{2}$. Given pore density function $\gamma(z)$, the cell width in row n equals $w_n=\frac{1}{\sqrt{\gamma(z_n)}}$. Therefore, one can sequentially compute the width of each layer by

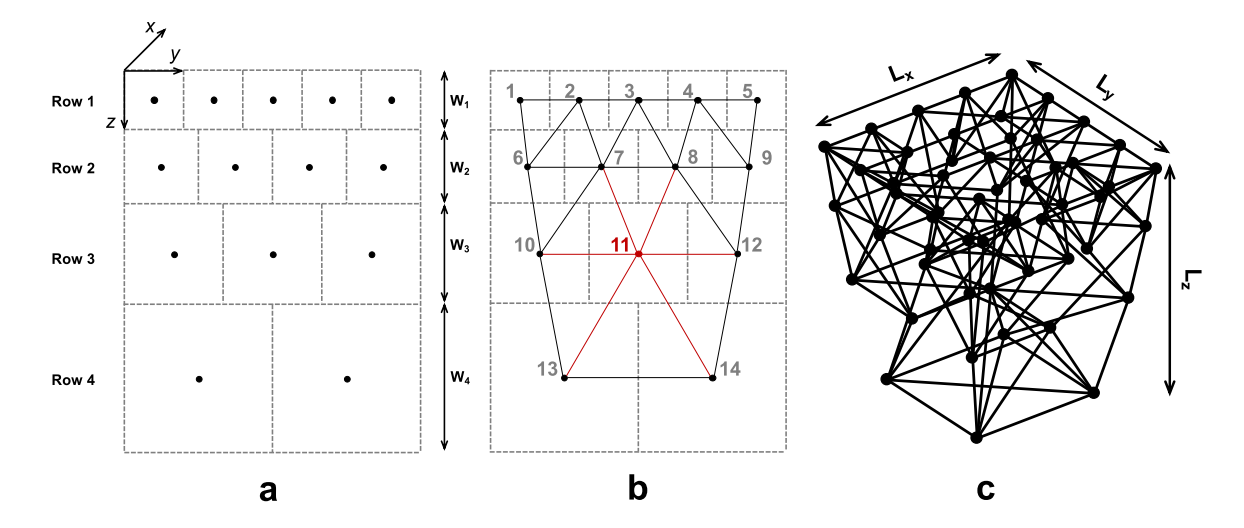


Fig. 2. Pore network generation with prespecified pore density profile and coordination number: (a) two-dimensional view of cubic grid (dashed gray) with the location of pore bodies (filled black circles). (b) Fully connected pore network. Solid lines represent the links (pore throats). (c) Three-dimensional pore network with target coordination number of 6 for all nodes. The achieved average coordination number of the network is ~6.2.

solving the following implicit equation for w_n :

$$w_n = \frac{1}{\sqrt{\gamma \left(\sum_{i=1}^{n-1} w_i + \frac{w_n}{2}\right)}} \tag{1}$$

Once the width of each layer is determined, we proceed by populating each layer with cubic cells of width w_n . In the resulting cubic grid, the pore bodies (nodes) will be located at the cell centroids. The next step is to connect each node to all its adjacent nodes. The fully connected network for the cubic grid in Fig. 2a is shown in Fig. 2b. Given an arbitrary pair of nodes i and j, there can exist a link e_{ij} if the corresponding cubic cells of nodes i and j fully or partially share a vertex, an edge or a face (e.g., node 11 is connected to nodes $\{7, 8, 10, 12, 13, 14\}$ because the cubic cell of node 11 is touching the cubic cells of nodes $\{7, 8, 10, 12, 13, 14\}$).

Finally, to reach the desired coordination number distribution, we need to randomly remove the extra links. The link removal method used in this study is inspired by Ben-Avraham et al.'s method of generating scale-free random spatial graphs with target degree distribution [22]. Given the fully connected network and the target coordination number distribution $P(\lambda)$, a coordination number $\lambda_{target,i}$ is assigned to each node iin the network. The assigned values are shuffled to make sure the target coordination number λ_{target} for each node does not exceed its current coordination number $\lambda_{current}$. Randomly going over the nodes in the network, if $\lambda_{target,i} < \lambda_{current,i}$, all links $\{e_{ij}\}$ for node i are listed, where index j refers to the index of a neighboring node. From the $\lambda_{current,i}$ links listed in $\{e_{ij}\}$, only the links (e_{ij}) with $\lambda_{target,j} < \lambda_{current,j}$ are kept. Then, $\lambda_{current,i} - \lambda_{target,i}$ randomly selected links in $\{e_{ij}\}$ are removed from the network. At this point the $\lambda_{current}$ for node i and its neighboring nodes jneeds to be updated. This process is repeated for all the nodes in the network. The resulting network will have a coordination number distribution close to the target coordination number distribution. Fig. 2c illustrates a 3D network with target coordination number of 6 and achieved average coordination number of \sim 6.2.

Once the pore networks for the top separation layer and substructure are generated, these networks are assembled by laying the separation layer network over the substructure network and connecting adjacent pore bodies *via* interface pore throats (links). We assume full connectivity between the two layers (*i.e.*, no links are removed after all the pores at the top of the substructure network are connected to the pores at the bottom of the separation layer network). An example of interface links is shown in Fig. 7c.

2.5.2. Permeability simulation

To compute membrane permeability, a pressure-driven steady state flow is simulated in the pore network by assigning inlet pressure (P_{inlet}) and outlet pressure (P_{outlet}) boundary conditions to the top of the separation layer and the bottom of the substructure, respectively, where $P_{inlet} > P_{outlet}$. No-flow condition is assigned to all other boundaries. Assuming incompressible flow, mass of the fluid at each pore body is conserved. Therefore, for each pore body i with coordination number λ_i , we have:

$$\sum_{i} q_{ij} = 0 \tag{2}$$

where q_{ij} is the steady state flow from pore body i to any neighboring pore body j through pore throat ij. The steady state flow between pores i and j is assumed to follow the Hagen-Poiseuille law, therefore:

$$q_{ij} = K_{ij} (P_i - P_j), K_{ij} = \frac{\pi D_{ij}^4}{128\mu L_{ij}}$$
(3)

where, for pore throat ij, K_{ij} is the hydraulic conductance, D_{ij} is the diameter and L_{ij} is throat length. P_i and P_j refer to the fluid pressures at pore bodies i and j, respectively, and μ is fluid viscosity. Solving the

resulting system of linear equations, the pressure at each pore body is computed. The overall flow rate Q can then be calculated by summing all the flows at either the network inlet or outlet. Finally, the absolute permeability can be calculated as:

$$k = \frac{Q}{A(P_{inlet} - P_{outlet})} \tag{4}$$

where k is absolute permeability in LMH/bar and A is the cross-sectional area of the membrane network model.

2.5.3. Input data for pore network modeling

As described in the previous sections, to construct a stochastic pore network and compute permeability, input data are needed. Although acquiring all this information directly *via* imaging is preferable, 2D SEM images do not provide any information on the 3D membrane structure. To this end, 3D substructural information is extracted from the 3D tomographic reconstruction of a polymeric scaffold acquired in an earlier study [23]. The 3D structures of the hierarchical polymeric scaffold and the SNIPS membrane substructure are assumed to be similar, as both are formed *via* spinodal decomposition. Detailed analysis of the 3D tomographic reconstruction of this polymer scaffold is presented in Appendix C. The rest of this section discusses the input parameters and assumptions made for each membrane layer.

Pore density is assumed to be constant throughout the separation layer and was calculated from top surface SEM images. The 2D square-packed top surface pore geometry and interconnected pore network suggest that the separation layer is a simple cubic lattice. The coordination number is assumed to be constant and equal to six, where each pore is only connected to its six closest neighbors. In other words, a pair of pores is connected only if the associated cubic cells share a face. The pore size distribution, also derived from top surface SEM images, is assumed to follow a normal distribution. These pore diameters are assigned to the pore bodies in the network and the equivalent pore throat diameters are assumed to be the harmonic mean of the associated pore bodies. The length of each pore throat is assumed to be the Euclidean distance between the associated pore bodies. Separation layer thickness is estimated from the cross-sectional SEM images.

The substructure pore density function, pore size distribution, and thickness are derived from 2D cross-sectional SEM images. The coordination number distribution is assumed to be the same as that of the block copolymer scaffold analyzed in Appendix C. Assignment of (equivalent) pore diameters to pore bodies and pore throats was performed as detailed previously for the separation layer. To account for the tortuosity of microstructure, the length of each pore throat is assumed to be 1.265 times the Euclidean distance between the associated pore bodies (Appendix C).

2.6. Macropores vs mesopores

To perform a meaningful flow simulation, it is essential to differentiate between the macropores and mesopores within the substructure, so that mesopores that are not connected to the macroporous network are not included in the pore network construction.

Fig. 3a shows two large macropores (lined in red) within the substructure that are separated by a mesoporous wall of thickness $2 \times b$. The pores decorating this mesoporous wall (e.g., see Fig. 1d) are connected to adjacent macropores via mesopores that are orders of magnitude smaller than said macropores. Including either of these mesopore types in the SPNM flow simulation may cause significant underestimation of permeability. Performing a meaningful flow simulation thus relies upon differentiating between macropores and mesopores so that the latter is excluded from pore network construction.

A closer look at the walls of a macropore (Fig. 1d) reveals a relatively ordered array of nanoscale pores (mesopores), much like those populating the membrane top surface. We also observe larger mesopores in

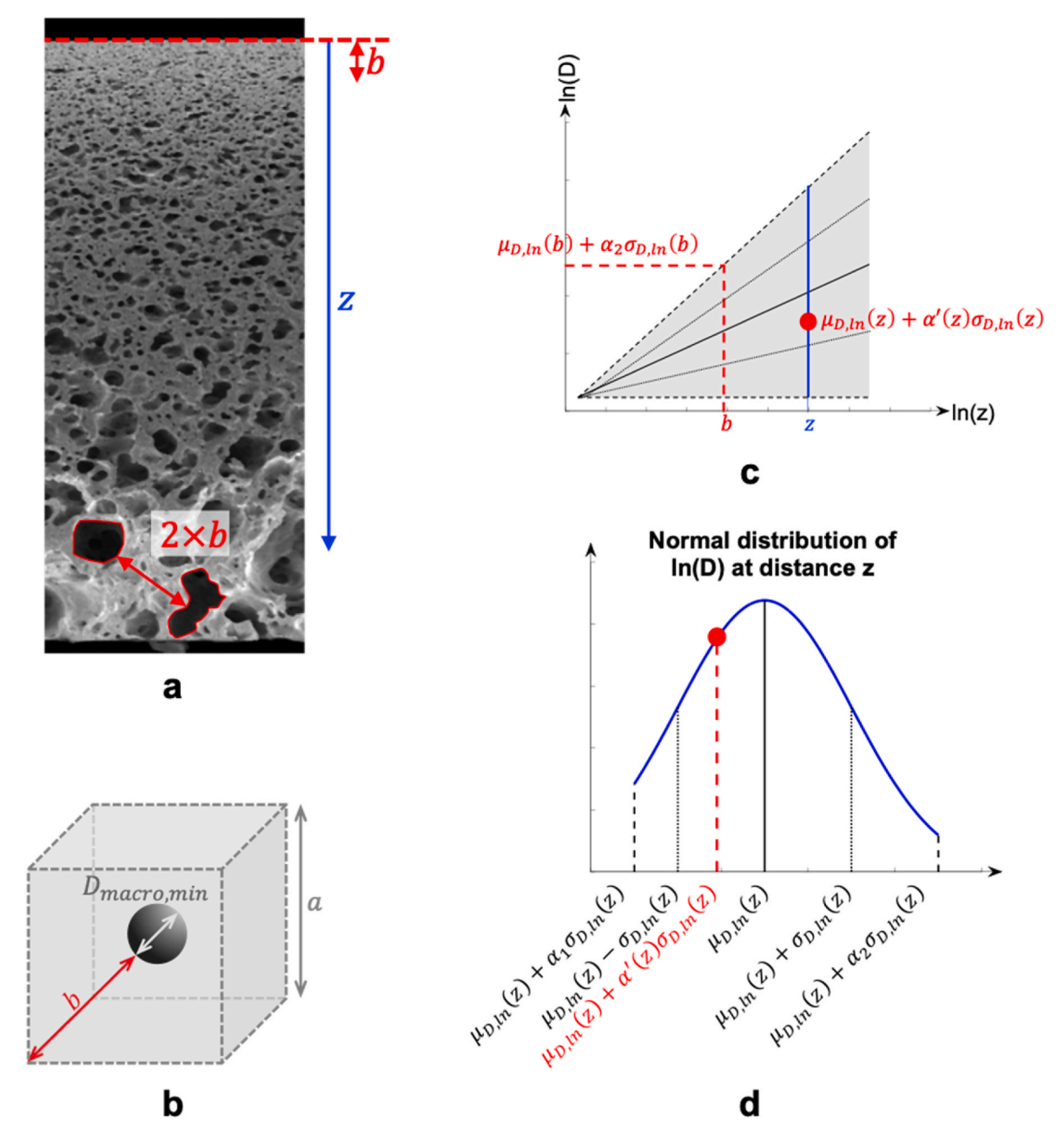


Fig. 3. (a) Example of two macropores within the membrane substructure. Distance between these macropores is denoted as $2 \times b$ (b) Schematic of one macropore from (a) contained within its cubic cell, as represented in the pore network model. (c) Schematic of overall substructure pore size distribution in log-log scale. Blue line marks an arbitrary location at depth z from the top of the membrane. (d) Schematic of truncated normal distribution of \mathbf{ln} (D) for the arbitrary location shown in (c).

2D SEM images (e.g., see pores that appear between the two macropores marked in Fig. 3a). Based on these observations, we hypothesize that the structure of the mesoporous walls extends throughout the entirety of the membrane: on the surface of the wall, pores sizes are similar to those of separation layer pores; and as wall thickens, larger pores appear within the wall. In other words, at some distance z away from the separation layer, thin mesoporous walls with ordered pore structure transition to thicker porous walls that contain larger pores. Following this rationale, we assume that the structure of all porous walls is the same throughout the membrane, *i.e.*, if the wall (denoted by the double-headed arrow in Fig. 3b) has a half-thickness b, its structure is identical to the top section of membrane with thickness b.

To formulate this hypothesis, it is essential to examine the pore size distribution in the substructure. As will be shown in the Results section,

at each depth z, the pore diameter distribution can be estimated using a truncated lognormal distribution. It will also be shown that the mean and standard deviation of the natural log of pore diameters increases linearly with $\ln(z)$. Therefore, the overall pore size distribution and pore size gradient resemble the gray region shown in Fig. 3c, where the solid line is the mean of the natural log of pore diameter $\mu_{D,ln}(z)$, dotted lines show one standard deviation, $\sigma_{D,ln}(z)$, away from $\mu_{D,ln}(z)$, and the dashed lines show the truncation limits, namely $\mu_{D,ln}(z) + \alpha_1 \sigma_{D,ln}(z)$ and $\mu_{D,ln}(z) + \alpha_2 \sigma_{D,ln}(z)$. The truncated lognormal distribution at location z is shown in Fig. 3d.

Let's assume that at each depth z, there is a sharp threshold diameter $D^{'}(z)$ that marks the transition from mesopores to macropores (red circle in Fig. 3c and d). This assumption naturally means that $D^{'}(z)$ equals the diameter of the smallest macropore at depth z ($D_{min,macro}(z)$). Let's define

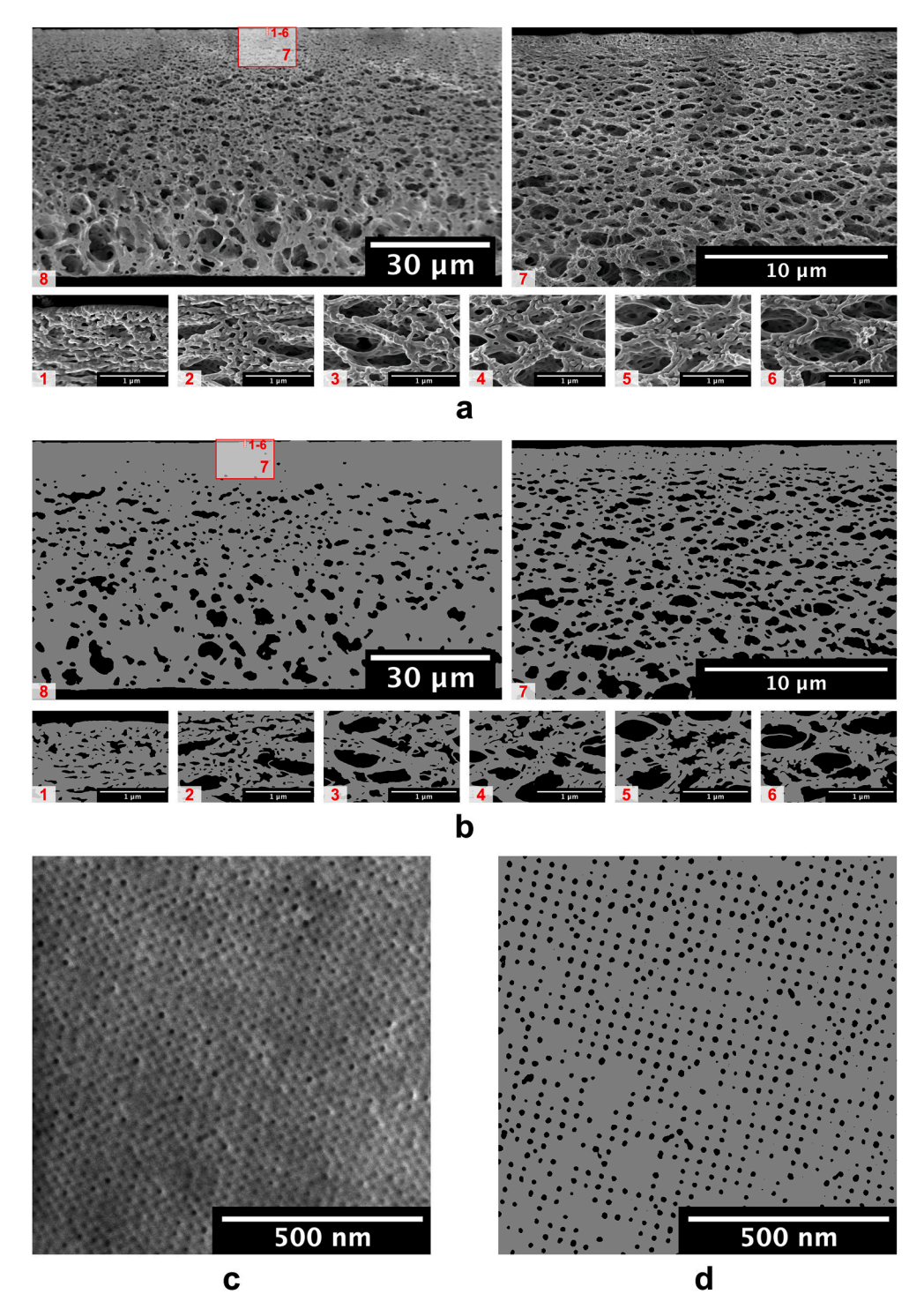


Fig. 4. (a) Cross-sectional SEM images for ISV87. Image 8 shows the entire membrane cross-section. Shown in numbered red boxes are the approximate locations of SEM images with higher resolution. (b) The segmented images corresponding to SEM images in (a). Gray pixels show the solid matrix and black pixels show the void space. (c) Top-view SEM image of separation layer. (d) Segmented image of SEM image shown in (c).

$$D_{min,macro}(z) = exp\left(\mu_{D,ln}(z) + \alpha' \sigma_{D,ln}(z)\right)$$
(5)

where $\alpha_1 < \alpha' < \alpha_2$. The threshold diameter $D^{'}(z)$ also equals the largest mesopore at depth z, which will exist in the thickest porous wall available at depth z. Following the proposed algorithm for pore network generation, each macropore at distance z is contained in a cubic cell of width $a=1/\sqrt{\gamma(z)}$ (Fig. 3b). Given this assumption, the thickest porous wall that can be formed at distance z has a half-width of $b=\frac{\sqrt{3}}{2}a$

 $\frac{D_{min.macro}}{2}$. If the structure of porous walls is the same throughout the entire membrane, then the diameter of the largest mesopore $(D_{max,meso}(z))$ becomes:

$$D_{max,meso}(z) = exp(\mu_{D,ln}(b) + \alpha_2 \sigma_{D,ln}(b))$$
(6)

depicted by the dotted red line in Fig. 3c. Since $D_{min,macro}(z) = D_{max,meso}(z)$, one can iteratively solve for $\alpha^{'}$ and subsequently $D^{'}(z)$. Repeating this process for all z values provides the pore size threshold as a function of z.

3. Results

As described in Sections 2.1-2.2, two ISV SNIPS membranes, namely ISV87 and ISV138, were made and characterized *via* SEM. While this section focuses on the analysis of ISV87, the same approach was applied to ISV138 (Appendix A).

3.1. Image segmentation

Fig. 4a shows two-dimensional cross-sectional images of an ISV87 membrane at different resolutions, and Fig. 4c shows the corresponding top surface SEM image. To understand the structure of this membrane, we first need to segment the images. The image segmentation algorithm used in this study is the supervised continuous max-flow and min-cut algorithm [24–26] described in Appendix B. Fig. 4b and d show the segmentations corresponding to the SEM images shown in Fig. 4a and c, respectively. Comparing the original images and the segmented images shows that given sufficient image resolution, the supervised continuous max-flow and min-cut algorithm is able to isolate the pores from the solid matrix.

3.2. Pore size distribution

Once the images are segmented, the hydraulic diameter $(D_H = \frac{4A}{p})$ for each pore is recorded, where A is the pore's area and p is its perimeter. Top surface SEM image analysis of the ISV87 membrane (Fig. 4d) reveals a normal distribution for pore diameters with mean of 13.16 nm and standard deviation of 2.75 nm.

Cross-sectional SEM images (Fig. 4b) were then used to determine the pore size distribution of the substructure. Resolution limitations led to a minimum detectable pore size at each magnification. Fig. 5 shows a clear gradient in D_H as a function of distance between the pore centroid and the top of the membrane (z). This gradient is also evident in image 7 (Fig. 4a and b). Analyzing the datapoints for images 7–8 reveals that, for $\ln (D_H)$ vs. $\ln(z)$: (1) the pore size distribution at each distance z resembles a truncated lognormal distribution and (2) a linear fit for mean and standard deviation is sufficient to capture the pore size gradient in each of these images. As the mean and standard deviation curve slopes

do not change significantly across images 7–8, it was concluded that, in log-log scale, the mean and standard deviation curves for the overall pore size distribution have the same slopes as in images 7–8. In this study, the image with the lowest resolution (image 8) was used to find the mean and standard deviation curve slopes. The intercept was assumed to be the mean and standard deviation of D_H in image 1. In Fig. 5, the solid black line represents the mean curve for all pores, the dotted black lines denote one standard deviation above and below the mean curve, and dashed black lines denote the upper and lower truncation limits. As this analysis was performed on a logarithmic scale, the pore size distribution at each depth z is a truncated lognormal distribution on the linear scale.

At this point, the determined pore size distribution includes both macropores and mesopores. For SPNM simulation, however, we only need the pore size distribution of macropores. Following the reasoning in Section 2.6, the mesoporous threshold diameter D'(z) (Fig. 5, dashed red line) is found for this membrane. The red circle marks the depth $z=2.74~\mu m$, below which the porous wall is completely ordered, consistent with the transition from single-layer walls to thicker walls between $z\approx 2-3~\mu m$ in SEM images 2–3 (Fig. 4a). Here we assume that the substructure pore size distribution and pore density stay constant below this depth. At $z\approx 2.74~\mu m$, the diameter threshold (D_H) is 58 nm, which, according to our hypothesis, corresponds to the average pore diameter of the ordered porous wall sections. Our measurements of pore sizes on the surface of porous walls (not presented here) reveal a similar diameter.

3.3. Pore density profile

Analyzing the ISV87 membrane top surface (Fig. 4d) reveals a pore density of $8.97 \times 10^{14} \ pores/m^2$.

Considering that the pore density profile for all ISV87 cross-sectional images is consistent with an exponential decay function, we assume that pore density function for the entire substructure is also an exponential decay. As shown in Fig. 6, seven datapoints are used to fit the exponential decay function: overall pore density in images 1–6 and corrected pore density for the lower 10 μm in image 8. The correction accounts for the resolution-limited missing pore size data and is calculated: (1) based on the truncated lognormal pore size distribution assumption, and (2) by

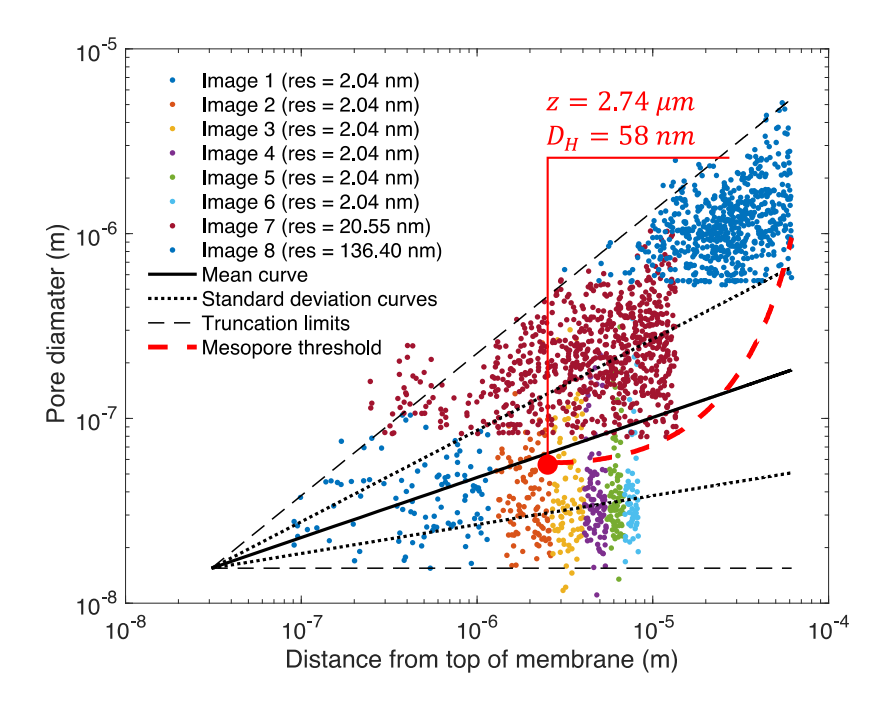


Fig. 5. Pore size distribution for ISV87. Both axes are in logarithmic scale. The scatter datapoints show the hydraulic diameter (D_H) vs. distance between the centroid of the pore to the top of the membrane (z). Solid black line shows the mean curve, dotted black lines show one standard deviation above and below the mean curve, and dashed black lines show the upper and lower truncation limits of all pores (macropores and mesopores). The threshold between meso- and macropores is shown by the red dashed line. The solid red circle shows the depth below which the mesoporous wall is completely ordered.

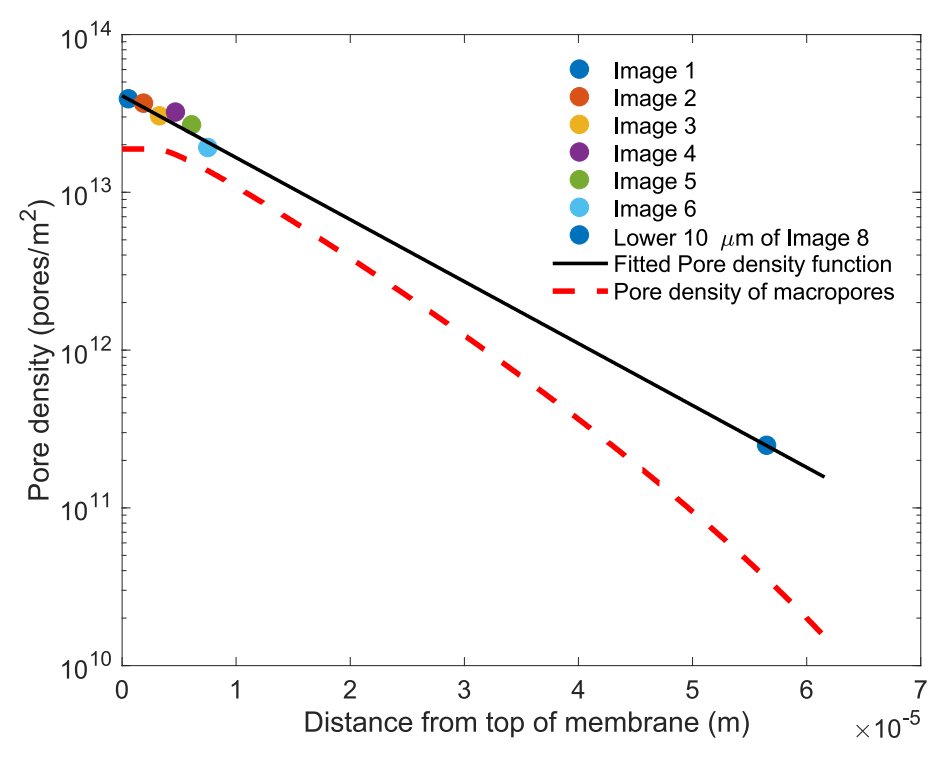


Fig. 6. Pore density profile for substructure of ISV87. The vertical axis is in logarithmic scale. Individual datapoints represent the pore densities in images 1–6 as well as the corrected pore density for the lower $10 \mu m$ in image 8. The black solid line is the overall pore density profile of the substructure. The red dashed line is the corrected pore density profile reflecting only macropores.

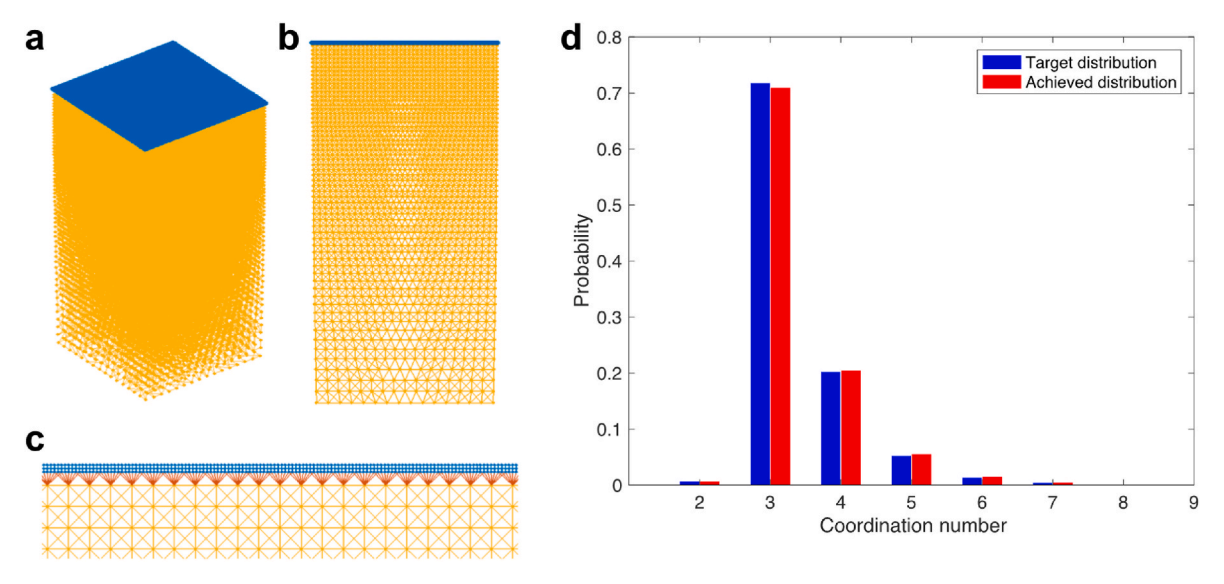


Fig. 7. Pore network generation for ISV87. (a) 3D view of a $10 \times 10 \times 20 \,\mu m$ pore network. (b) 2D side view of the network. (c) Zoomed-in view of the separation layer network and interface links (red). (d) comparison between the target and achieved coordination number distribution for the substructure.

accounting for the area under the lognormal curve that is not covered by measured pore diameters in image 8. The solid black line in Fig. 6 shows the resulting pore density profile $\gamma(z)$.

As was the case with the pore size distribution, the current pore density profile includes both macro- and mesopores. To find the pore density profile of macropores, we use the mesopore diameter threshold in Fig. 5 (red dashed line) as the lower truncation limit of the pore size distribution to remove the mesopore area fraction under the lognormal curve. The red dashed line in Fig. 6 shows the corrected pore density profile for just macropores. Pore density was assumed to be constant below $z\approx 2.74~\mu m$, consistent with prior analysis of pore size

distribution.

3.4. Pore network generation

Using the SEM images of ISV87, the thickness of the separation layer and the entire membrane are measured as $\sim 100 \, nm$ and $\sim 62 \, \mu m$, respectively. Given the calculated pore density profile and the algorithm in Section 2.5, a two-layer pore network model is generated. Fig. 7a–c shows a portion of the generated pore network. The comparison between the target and achieved coordination number distribution is shown in Fig. 7d. From this figure, the proposed link removal algorithm

closely matches the target coordination number distribution.

3.5. Permeability simulation

Absolute permeability is simulated for ISV87 for a range of cross-sectional areas starting from 4 $\mu m \times$ 4 μm . Incremental increases revealed that a cross-sectional area of 10 $\mu m \times$ 10 μm was sufficient to represent the membrane. The calculated absolute permeability, based on SPNM, was 371.58 \pm 6.70 LMH/bar, which underestimates the experimental value of 484 \pm 66 LMH/bar by \sim 23%.

3.6. Sensitivity analysis

As shown in Fig. 4c and d, the segmentation algorithm identifies some of the main pores in the top separation layer (*i.e.*, pores constituting the square lattice formation) as blocked pores, while detecting additional smaller pores that are located at the center of these square lattices. We will refer to these smaller pores as indents. Although there is no straightforward approach to experimentally examine whether a pore is blocked or open, it is normal to observe such artifacts in any segmentation method.

As these artifacts could significantly alter the pore density and pore size distribution, and thus the simulated permeability, it is crucial to understand the sensitivity of the SPNM model to changes in these top separation layer parameters. To perform a meaningful sensitivity analysis, a reference case is defined based on the assumption that all pores constituting the square lattice are open and all indents are blocked (or solid). Based on this assumption, the top separation layer pore density is $\sim 9.18 \times 10^{14} \, pores/m^2$. The corresponding pore size distribution was determined by fitting the raw pore diameter measurements with a bimodal normal distribution (vs. a regular normal distribution), and discarding the distribution with the smaller mean value, yielding $13.90 \pm 1.72 \, nm$. Using SPNM in conjunction with these updated values only results in a 5% increase in simulated permeability to $390.68 \pm 7.90 \, LMH/bar$ ($\sim 19\%$ lower than the measured permeability).

Based on the reference case (*vide supra*), two numerical experiments were designed to study the effects of mean pore diameter and pore density of top separation layer on simulated permeability in further detail. In the first experiment (Fig. 8a), the pore diameter distribution of $13.90 \pm 1.72 \, nm$ (denoted by a solid black marker) is used as the reference and the incrementally increased/decreased mean pore diameter is used as the input for SPNM. As shown in this figure, for small pore diameters, a slight change in the mean pore diameter can significantly change the simulated permeability (*e.g.*, decreasing the mean pore diameter by 30%, from 13.90 nm to 9.73 nm, results in a 45% reduction in permeability). However, once the mean diameter reaches $\sim 35 \, nm$,

permeability levels off at ~ 550 *LMH/bar*. According to this analysis (all else held constant), a mean pore diameter of 18.61 nm is needed to match the mean experimental permeability (484 LMH/bar). The 4.71 nm difference (18.61 nm vs. 13.90 nm) is equivalent to ~ 3.65 pixels.

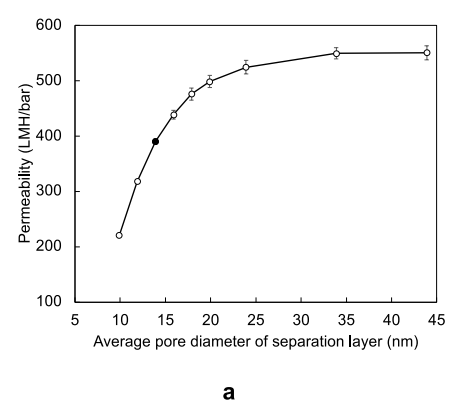
The second experiment (Fig. 8b) simulates the effect of blocked pores on the simulated permeability. To that end, the reference pore density of $9.18 \times 10^{14} \, pores/m^2$ (0% blocked pores, denoted by a solid black marker) is incrementally decreased to reflect the increased fraction of blocked pores. Comparing Fig. 8a and b, the simulated permeability is less sensitive to changes in pore density than pore diameter. For instance, 20% decreases in pore density (from $9.18 \times 10^{14} \, \frac{pores}{m^2}$ to $7.34 \times 10^{14} \, \frac{pores}{m^2}$) and mean pore diameter (from $13.90 \, nm$ to $11.12 \, nm$) result in 11% and 28% decreases in permeability, respectively.

4. Discussion

This work was inspired by challenges in characterization and flow simulations in BCP SNIPS ultrafiltration membranes. Our goals were to develop (1) a method to delineate the hierarchical asymmetric BCP membrane pore structure, and (2) a fast method for pore-scale modeling of flow in these membranes. To achieve the first goal, we developed a procedure that uses segmented 2D top separation layer and substructure SEM images to delineate the 3D hierarchical membrane pore structure. To achieve the second goal, the resulting pore size distribution was used as the input for an asymmetric SPNM, which was then employed to estimate absolute membrane permeability. The results are very promising.

Several assumptions have been made throughout the analysis. Given the lack of a high-resolution 3D membrane reconstruction, this study used 2D SEM images. Therefore, assumptions were made to account for the missing information from the third dimension. It was assumed that the pore structure in the *xy*-plane at each depth *z* is the same as what we observe in cross-sectional images. For instance, images 1 and 7 (Fig. 4) reveal that the pores are compressed near the top surface of the ISV87 membrane. Using pore sizes acquired from segmenting these cross-sectional images, the same compression was assumed to exist in that entire section, in all directions, which may have resulted in an underestimation of permeability for ISV87. To relax this assumption, one needs to acquire 2D images of the membrane etched parallel to the top surface.

Acquiring more 2D images would also enable the digital reconstruction of the 3D membrane structure. Image reconstruction has been used extensively as a cost-effective alternative to 3D imaging [27,28]. Particularly with the recent advances in computer vision and artificial intelligence (AI), more sophisticated porous media image reconstruction methods have been developed in the past few years [29]. If successful,



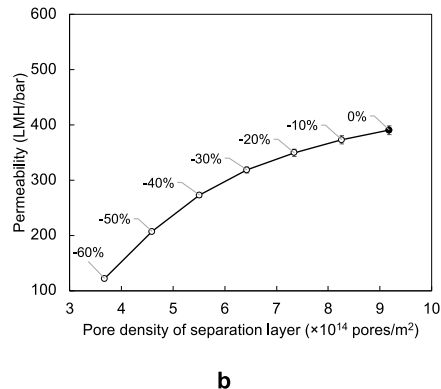


Fig. 8. Simulated permeability of ISV87 membrane as a function of (a) average pore diameter and (b) pore density of top separation layer. Black markers in (a) and (b) denote the reference permeability value of $390.68 \pm 7.90 \, LMH/bar$ simulated using pore diameter distribution of $13.90 \pm 1.72 \, nm$ and pore density of $9.18 \times 10^{14} \, pores/m^2$, respectively. Data labels in (b) show the percentage decrease in pore density (*i.e.*, the fraction of blocked pores).

the 3D reconstructed image would not only enable us to re-examine the assumptions made on pore shape, length, and connectivity, but it could also be used as input to more accurate, topologically-consistent pore-scale flow modeling.

Segmenting SEM images also comes with a set of assumptions. For instance, the choice of thresholds (discussed in Appendix B) is highly user-dependent. Slight threshold alterations naturally result in different pore size estimations and therefore permeability values. Our sensitivity analysis presented in Section 3.6 (and Appendix A) also confirms that even a few pixels' difference in pore diameter measurement could lead to significant change in simulated permeability. In addition, when a large pore is detected and isolated during the segmentation process, smaller low-intensity pores that are within the large pore will be neglected. A more sophisticated image processing technique may alleviate this drawback.

In this study, we assume that the membrane structure is rigid, and permeability is independent of applied pressure. However, prior work by Zhang et al. [8] showed that higher applied pressures potentially lead to membrane compression and decreased permeability.

To find the threshold between macropores and mesopores, a hypothesis was presented in Section 2.6, in which we assumed that the structure of all porous walls is the same throughout the entire membrane. Although the result of the hypothesis is consistent with the observations from SEM images, acquiring high-resolution images from the lower half of the substructure will help substantiate/improve this hypothesis.

The pore network model of the membrane assumes constant thickness for the separation layer, while both Fig. 4 and Fig. A1 show slight variation in its thickness. Because of the high sensitivity of computed permeability to properties of the separation layer discussed in Section 3.6 and Appendix A, incorporating this variation could help improve the predictability of the SPNM model. In addition, it was assumed that the effect of mesopores on membrane permeability is negligible. Future work will utilize a two-scale pore network model like [30] to examine the validity of this assumption.

The ultimate objective of this work is to create efficient processes to design and synthesize ultrafiltration membranes tailored for specific applications. Currently, designing ultrafiltration membranes with targeted properties is an expensive procedure that relies heavily on prior experience and lengthy trial-and-error procedures. Surmounting these obstacles requires understanding the relationships between synthesis parameters, membrane structure, and their effective properties [31]. We envision this work and subsequent studies will help elucidate these relationships.

5. Conclusions

In this study, we proposed a novel simple method to compute the absolute permeability of BCP SNIPS ultrafiltration membranes. First, we used 2D SEM images with a variety of resolutions to delineate the hierarchical asymmetric pore structure. Next, to simulate flow, a novel stochastic pore network model was proposed and employed to compute absolute permeability of two ultrafiltration membranes. Our comparison showed good agreement between simulated and measured permeabilities.

Author statement

M. Sadegh Riasi: Conceptualization, Methodology, Software, Writing - original draft, Writing - review & editing. Lieihn Tsaur: Conceptualization, Investigation, Validation, Writing - original draft, Writing - review & editing. Yuk Mun Li: Investigation, Writing - review & editing, Qi Zhang: Investigation, Writing - review & editing, Ulrich Wiesner: Supervision, Funding acquisition, Conceptualization, Writing - review & editing, Lilit Yeghiazarian: Supervision, Funding acquisition, Conceptualization, Writing - review & editing.

Declaration of competing interest

U.W. is a co-founder of TeraPore Technologies, Inc., a company commercializing block copolymer SNIPS derived ultrafiltration membranes.

Data availability

Data will be made available on request.

Acknowledgements

L.Y. would like to gratefully acknowledge the National Science Foundation for supporting this research (CBET-1351361). U.W. would also like to acknowledge funding by the National Science Foundation (DMR-1707836). The authors would like to thank Dr. Rachel Dorin for providing the block copolymer ISV87, and Dr. Hiroaki Sai for providing the data used in Appendix C. The authors also would like to thank Dr. S. Majid Hassanizadeh and Dr. Matthijs de Winter for the fruitful discussion during InterPore 2021 conference as well as their suggestions on how to improve the work in future. Finally, we would like to thank the anonymous reviewers for insightful comments on the manuscript.

Appendix A. Data and analysis of ISV138

SEM images for ISV138 were segmented and associated pore size distributions and pore density profiles were extracted as previously detailed for ISV87. Figure A1 shows the original and segmented SEM images for ISV138. In addition to a top surface SEM image of the top separation layer (Fig. A1c-d), 7 cross-sectional SEM images were acquired for the substructure of the membrane (Fig. A1a-b).

The pore density of the top separation layer is calculated as 7.17×10^{14} *pores*/ m^2 and its pore diameter distribution is assumed to be a normal distribution with a mean of 20.75 nm and standard deviation of 3.45 nm. Figures A2 and A.3 show the pore size distribution and pore density profile for ISV138, respectively. Pore size distribution and pore density profile were assumed to remain constant below $z = 2.35 \, \mu m$.

Using the SEM images of ISV138, the thickness of the separation layer and the entire membrane were measured as $\sim 130~nm$ and $\sim 50~\mu m$, respectively. Using SPNM and following the procedure described in Sections 3.4-3.5, the absolute permeability calculation resulted in 889.22 \pm 37.29 LMH/bar. Comparing with experimental values of 644 \pm 15 LMH/bar, SPNM overestimated the permeability by \sim 38%.

To study the effects of segmentation errors on the simulated permeability (as done for ISV87 in the main text), a reference case is defined for ISV138 and the sensitivity of the model to changes in pore size distribution and pore density is studied. The reference case for ISV138 comprises a pore density of 5.87×10^{14} pores/ m^2 and pore diameter normal distribution of 22.59 ± 2.15 nm. Using SPNM in conjunction with these adjusted values increases the simulated permeability by a meager 1.4% to 901.40 ± 41.32 LMH/bar (~40% higher than the measured permeability).

Figure A4 shows the results of the sensitivity analysis where the reference case is denoted by solid black markers. Consistent with the analysis of ISV87, the permeability of ISV138 is more sensitive to mean pore diameter than pore density. Based on Fig. A4a, to match the experimental mean permeability of 644 *LMH/bar*, a mean pore diameter of 16.50 *nm* is needed. Alternatively, the experimental measurement can be matched by SPNM if pore density is decreased by ~45% (Fig. A4b).

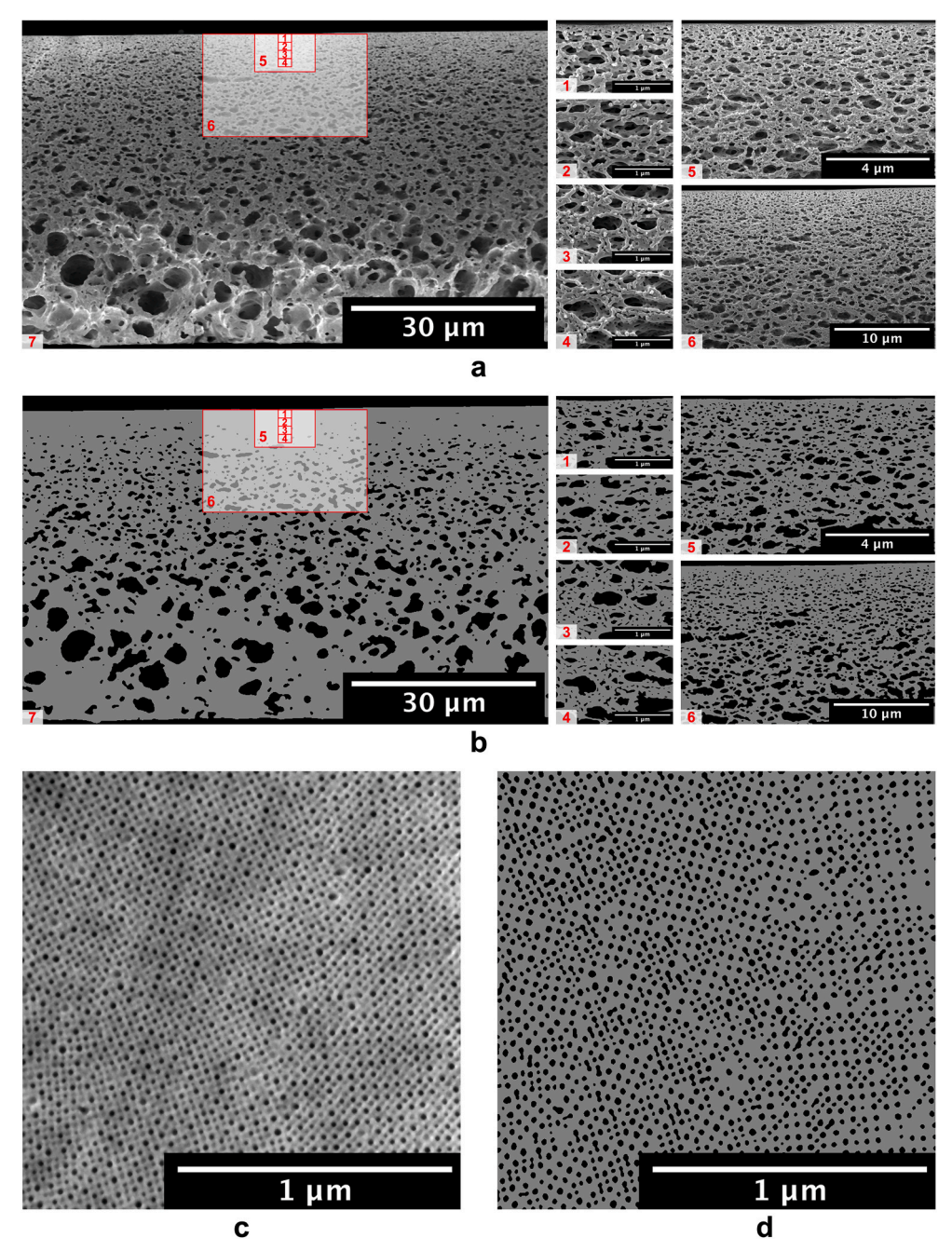


Fig. A.1. (a) Cross-sectional SEM images for ISV138. Image 7 shows the entire membrane cross-section. Shown in numbered red boxes are the approximate locations of SEM images with higher resolution. (b) The segmented images corresponding to the SEM images in (a). Gray pixels depict the solid matrix and black pixels the void space. (c) Top surface SEM image. (d) Segmentation of SEM image shown in (c).

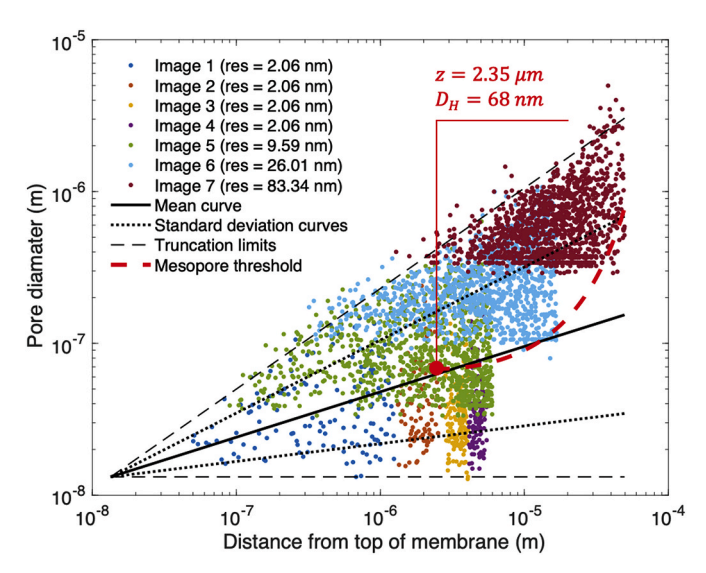


Fig. A.2. Pore size distribution for ISV138. Both axes are in logarithmic scale. The individual datapoints depict the hydraulic diameter (D_H) vs. distance between the centroid of the pore and the membrane top surface (z). Solid black line shows the mean curve, dotted black lines show one standard deviation above and below the mean curve, and dashed black lines show the upper and lower truncation limits of all pores (macropores and mesopores). The threshold between meso- and macropores is shown by the red dashed line. The solid red circle shows the depth below which the mesoporous wall is completely ordered.

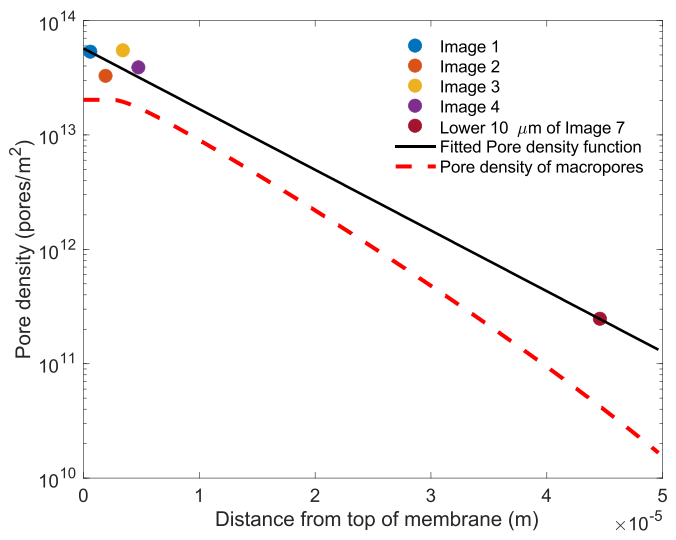


Fig. A.3. Pore density profile for substructure of ISV138. The vertical axis is in logarithmic scale. The individual datapoints represent the pore densities in images 1–4 as well as the corrected pore density for the lower 10 μm in image 7. The black solid line is the overall pore density profile of the substructure. The red dashed line is the adjusted pore density profile for only macropores.

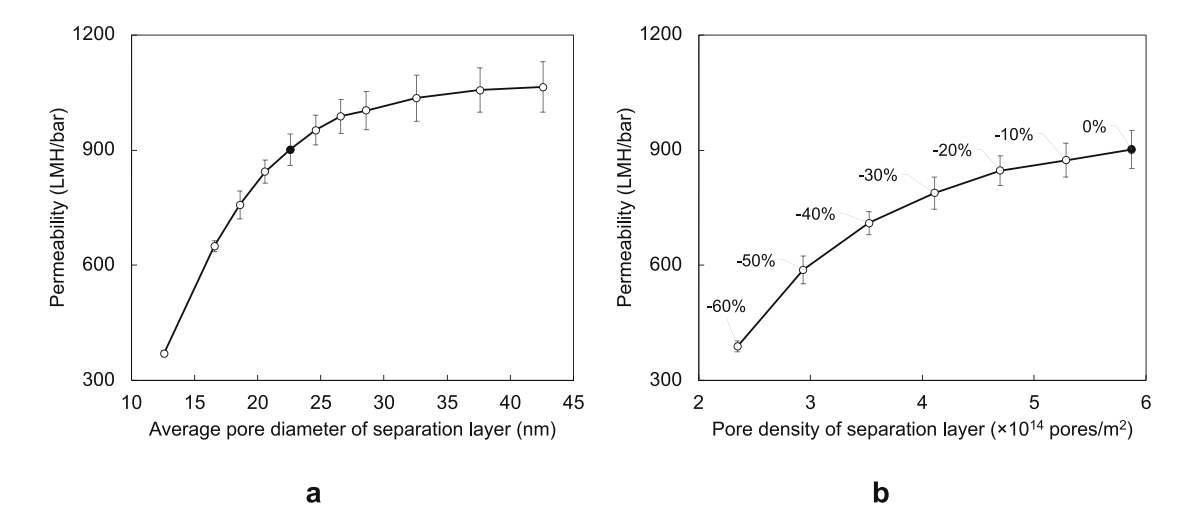


Fig. A.4. Simulated permeability of ISV138 membrane as a function of (a) average pore diameter and (b) pore density of separation layer. Solid black markers in (a) and (b) denote the reference permeability value of 901.40 ± 41.32 LMH/bar simulated using pore diameter distribution of 22.59 ± 2.15 nm and pore density of 5.87×10^{14} pores/m², respectively. Data labels in (b) show the percentage decrease in pore density (i.e., the fraction of blocked pores).

Appendix B. Continuous max-flow and min-cut algorithm

SEM images were segmented using a supervised continuous max-flow and min-cut algorithm [24–26]. Continuous max-flow segmentation is the continuous variation of the well-known graph-cut segmentation and is based on the dual problems of maximum-flow and minimum-cut in combinatorial graph theory. Much like any other segmentation method, continuous max-flow problems aim to partition a gray-scale image Ω into two disjointed regions, namely the foreground Ω_f and the background $\Omega_b = \Omega \setminus \Omega_f$.

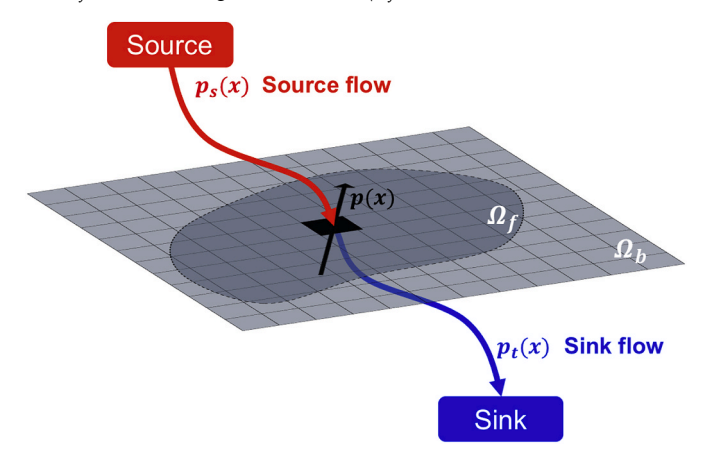


Fig. B.1. Schematic of continuous max-flow problem. Domain Ω represents a 2D gray-scale image where Ω_f is the foreground and Ω_b is the background. The dark square in the middle represents a pixel at location $x \in \Omega$. $p_s(x)$ and $p_t(x)$ are the source flow from source to position x and sink flow from position x to sink, respectively. p(x) is the spatial flow within the domain Ω .

As shown in Fig. B1, for a given image, let Ω be a continuous 2D domain where $x \in \Omega$ represents the location of pixels in the image and s and t are the source and sink terminals, respectively. Let p(x) be the spatial flow within the domain Ω at position $x \in \Omega$, and let $p_s(x)$ and $p_t(x)$ be the source flow from source to position x and sink flow from position x to sink, respectively. The supervised continuous max-flow model is then formulated as:

$$\max_{p_{s},p_{r},p} \int_{\Omega} u_{b}(x) \ p_{s}(x) \ dx - \int_{\Omega} u_{f}(x) \ p_{t}(x) \ dx$$

$$subject \ to: \ |p(x)| \le C(x), p_{s}(x) \le C_{s}(x), p_{t}(x) \le C_{t}(x), \text{div } p(x) - p_{s}(x) + p_{t}(x) = 0$$
(B.1)

where C(x), $C_s(x)$ and $C_t(x)$ are flow capacity functions. At each position x, C(x) is the flow capacity within the domain. $C_s(x)$ and $C_t(x)$ are the flow capacities for flow from the source and to the sink at position x, respectively. The equality condition in the optimization problem of Eqn B.1 is the flow conservation equation, and $u_f(x)$ and $u_b(x)$ are indicators that enforce the user-defined constraints of the foreground/background labels for specific pixels. These indicators can be defined as

$$u_f(x) = \begin{cases} 1, x \in \Omega_f \\ 0, x \notin \Omega_f \end{cases}, u_b(x) = \begin{cases} 0, x \in \Omega_b \\ 1, x \notin \Omega_b \end{cases}$$
(B.2)

It has been shown [24,26] that the max-flow problem of Eqn B.1 can be solved using its augmented Lagrangian function:

$$L_{c}(p_{s}, p_{t}, p, \lambda) = \int_{Q} u_{b}(x) p_{s}(x) dx - \int_{Q} u_{f}(x) p_{t}(x) dx + \int_{Q} \lambda [div p(x) - p_{s}(x) + p_{t}(x)] dx - \frac{c}{2} ||div p(x) - p_{s}(x) + p_{t}(x)||^{2}$$
(B.3)

where c > 0 and $\lambda \in [0, 1]$ is a multiplier. Solving the max-flow problem of Eqn B.3 will result in a λ map where each pixel is assigned a value between zero and one, representing the probability of that pixel belonging to the foreground. Therefore, the segmented image can be easily generated by thresholding the λ map with an arbitrary $\lambda_{threshold}$. For unsupervised max-flow problem, the indicators must be set to $u_f(x) = 0$ and $u_b(x) = 1$. The detailed algorithm on solving the max-flow problem described above can be found in Refs. [24,26].

In this study we propose the following steps:

- Step 1. If needed, crop the image to the region of interest.
- Step 2. Apply a 3×3 median filter.
- Step 3. Normalize the image. Let I(x) be the resulting matrix for the image.
- Step 4. Define the flow capacities as follows:

$$C_s(x) = |I(x) - (g_\rho * I(x) - 0.3)|$$

$$C_t(x) = |I(x) - (g_\rho * I(x) + 0.3)|$$

$$C(x) = 0.5$$
(B.4)

where g_{ρ} is a gaussian kernel with standard deviation of $\rho = 3$.

Step 5. Given two arbitrary scalar values $0 < t_2 < t_1 < 1$, define the indicators as follows:

$$u_f(x) = \begin{cases} 1, I(x) > t_1 \\ 0, I(x) < t_1 \end{cases}, u_b(x) = \begin{cases} 0, I(x) < t_2 \\ 1, I(x) > t_2 \end{cases}$$
(B.5)

In this study, we used Otsu's two-level thresholding technique to find t_1 and t_2 .

Step 6. Use I(x), C(x), $C_s(x)$, $C_t(x)$, $u_f(x)$ and $u_b(x)$ to solve the max-flow problem. The result of this step will be the multiplier $\lambda(x)$.

Step 7. Threshold λ using $\lambda_{threshold} = 0.5$. If $\lambda > \lambda_{threshold}$, the pixel belongs to foreground, *i.e.* the membrane matrix. Otherwise, the pixel belongs to void space.

Appendix C. BCP Pore structure analysis

The 3D tomographic reconstruction of a polymeric scaffold from an earlier study [23] was acquired and analyzed to extract information about the 3D structure of ISV membranes. We use Skeletonize3D and Analyze Skeleton plugins [32,33] in Fiji Image Processing Package [34–36] to extract and analyze the 3D skeleton (medial axis) of the void space of the polymeric scaffold.

Figure C1a shows the 3D structure of the polymeric scaffold in gray. Shown in red is the extracted medial axis of the void space. From the medial axis, one can construct an undirected graph network (Fig. C.1b) much like the pore networks generated in this study. The degree distribution of the graph network is used as the coordination number distribution in pore network modeling (Fig. C1c). To eliminate the effect of boundary nodes, nodes with coordination number of one are removed from coordination number analysis.

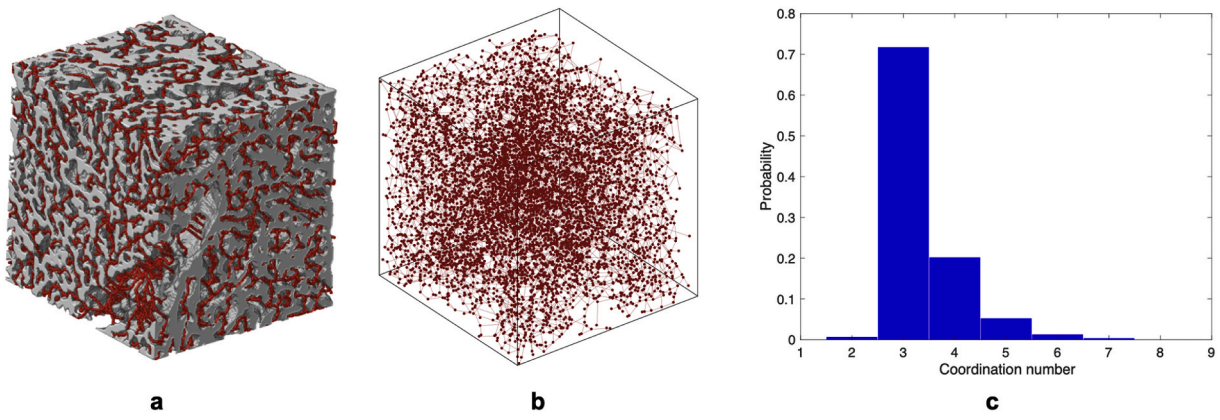


Fig. C.1. (a) 3D reconstruction of polymeric scaffold [23] shown in gray along with the extracted medial axis shown in red. (b) Graph network extracted from the medial axis. (c) Coordination number distribution of the extracted network.

Since the polymer scaffold has a disordered pore structure, the tortuosity of the pore throats needs to be accounted for. Figure C2a shows the relationship between the length of pore throats, computed from the medial axis, and the Euclidean distance between end-nodes. The linear fit shows that the average length of pore throats is \sim 1.265 times larger than their associated Euclidean length. We use this multiplier for all pore throats in the substructure portion of the membrane pore network.

Since we assume that the measured diameters from SEM images belong to the pore bodies in the network, a pore diameter must be defined for each pore throat as well. Using the extracted medial axis in Fig. C1a, the hydraulic conductance of each medial axis segment can be computed as described in an earlier study [37]:

$$k_{medial \ axis \ segment} = \frac{\pi}{128 \,\mu \, \int_0^L \frac{dx}{D(x)^4}} \tag{C.1}$$

where L is the length of medial axis segment in voxels and D(x) is the varying diameter of medial axis in voxels. Replacing the medial axis segment with an equivalent cylinder of length L and hydraulic conductance of $k_{medial axis segment}$, the equivalent diameter of the cylinder becomes:

$$D_{equivalent} = \left(\frac{L}{\int_0^L \frac{dx}{D(x)^4}}\right)^{1/4} \tag{C.2}$$

Red circles in Fig. C2b depict the equivalent diameters of pore throats with respect to the pore diameters of associated pore bodies. The gray surface represents the harmonic mean of diameters of each pair of pore bodies. As shown in this figure, a good correlation is observed. Therefore, the diameters of pore throats in the pore network model are assumed to be the harmonic mean of their corresponding pore bodies.

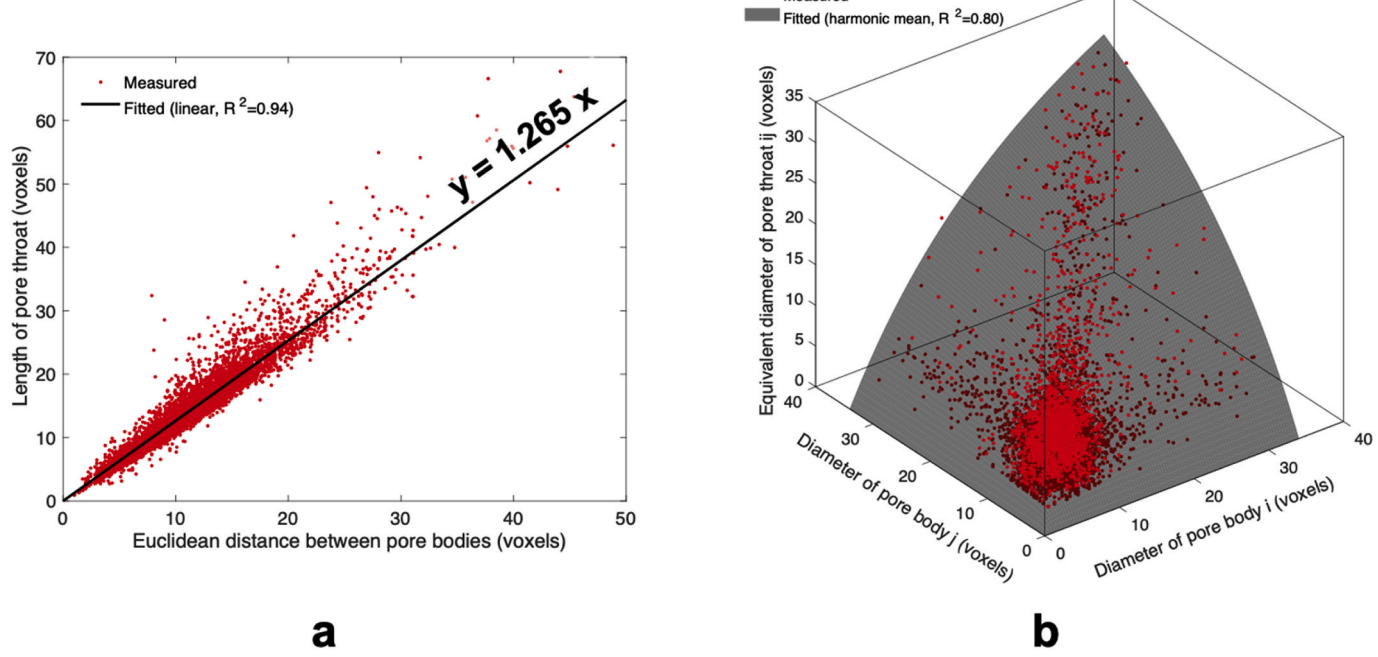


Fig. C.2. (a) Real length of pore throat vs. the Euclidean distance of end-nodes. Measured data shown in red. Solid black line represents the linear fit. (b) Equivalent diameters of pore throats vs. the diameters of the pore bodies at the end-nodes. Measured data shown in red. The gray surface represents the harmonic mean of the diameters of the pore bodies located at the end-nodes.

References

- M. Müller, V. Abetz, Nonequilibrium processes in polymer membrane formation: theory and experiment, Chem. Rev. 121 (2021) 14189–14231, https://doi.org/ 10.1021/acs.chemrev.1c00029.
- [2] S.P. Nunes, P.Z. Culfaz-Emecen, G.Z. Ramon, T. Visser, G.H. Koops, W. Jin, M. Ulbricht, Thinking the future of membranes: perspectives for advanced and new membrane materials and manufacturing processes, J. Membr. Sci. 598 (2020), 117761, https://doi.org/10.1016/j.memsci.2019.117761.
- [3] K.V. Peinemann, V. Abetz, P.F.W. Simon, Asymmetric superstructure formed in a block copolymer via phase separation, Nat. Mater. 6 (2007) 992–996, https://doi. org/10.1038/nmat2038.
- [4] R.M. Dorin, D.S. Marques, H. Sai, U. Vainio, W.A. Phillip, K.-V. Peinemann, S. P. Nunes, U. Wiesner, Solution small-angle X-ray scattering as a screening and predictive tool in the fabrication of asymmetric block copolymer membranes, ACS Macro Lett. 1 (2012) 614–617, https://doi.org/10.1021/mz300100b.
- [5] R.M. Dorin, W.A. Phillip, H. Sai, J. Werner, M. Elimelech, U. Wiesner, Designing block copolymer architectures for targeted membrane performance, Polym. (United Kingdom) 55 (2014) 347–353, https://doi.org/10.1016/j. polymer 2013.09.038
- [6] Y. Gu, U. Wiesner, Tailoring pore size of graded mesoporous block copolymer membranes: moving from ultrafiltration toward nanofiltration, Macromolecules 48 (2015) 6153–6159, https://doi.org/10.1021/acs.macromol.5b01296.
- [7] P. Vandezande, X. Li, L.E.M. Gevers, I.F.J. Vankelecom, High throughput study of phase inversion parameters for polyimide-based SRNF membranes, J. Membr. Sci. 330 (2009) 307–318, https://doi.org/10.1016/j.memsci.2008.12.068.
- [8] Q. Zhang, Y.M. Li, Y. Gu, R.M. Dorin, U. Wiesner, Tuning substructure and properties of supported asymmetric triblock terpolymer membranes, Polymer (Guildf) 107 (2016) 398–405, https://doi.org/10.1016/j.polymer.2016.07.076.
- [9] S. Mondal, I.M. Griffiths, G.Z. Ramon, Forefronts in structure–performance models of separation membranes, J. Membr. Sci. 588 (2019), 117166, https://doi.org/ 10.1016/j.memsci.2019.06.006.

- [10] M. Shi, G. Printsypar, O. Iliev, V.M. Calo, G.L. Amy, S.P. Nunes, Water flow prediction for membranes using 3D simulations with detailed morphology, J. Membr. Sci. 487 (2015) 19–31, https://doi.org/10.1016/j.memsci.2015.03.036
- [11] G. Sundaramoorthi, M. Hadwiger, M. Ben-Romdhane, A.R. Behzad, P. Madhavan, S.P. Nunes, 3D membrane imaging and porosity visualization, Ind. Eng. Chem. Res. 55 (2016) 3689–3695, https://doi.org/10.1021/acs.iecr.6b00387.
- [12] Y.M. Li, Q. Zhang, J.R. Álvarez-Palacio, I.F. Hakem, Y. Gu, M.R. Bockstaller, U. Wiesner, Effect of humidity on surface structure and permeation of triblock terpolymer derived SNIPS membranes, Polymer (Guildf) 126 (2017) 368–375, https://doi.org/10.1016/j.polymer.2017.05.037.
- [13] R.P. Castro, Y. Cohen, H.G. Monbouquette, The permeability behavior of polyvinylpyrrolidone-modified porous silica membranes, J. Membr. Sci. 84 (1993) 151–160. https://doi.org/10.1016/0376-7388(93)85057-4.
- [14] M.S. Riasi, N.K. Palakurthi, C. Montemagno, L. Yeghiazarian, A Feasibility Study of the Pore Topology Method (PTM), A Medial Surface-Based Approach to Multiphase Flow Simulation in Porous Media, vol. 115, Transp. Porous Media, 2016, pp. 519–539, https://doi.org/10.1007/s11242-016-0720-0.
- [15] X. Yang, Y. Mehmani, W.A. Perkins, A. Pasquali, M. Schönherr, K. Kim, M. Perego, M.L. Parks, N. Trask, M.T. Balhoff, M.C. Richmond, M. Geier, M. Krafczyk, L.-S. Luo, A.M. Tartakovsky, T.D. Scheibe, Intercomparison of 3D pore-scale flow and solute transport simulation methods, Adv. Water Resour. 95 (2016) 176–189, https://doi.org/10.1016/j.advwatres.2015.09.015.
- [16] T. Ramstad, C.F. Berg, K. Thompson, Pore-Scale Simulations of Single- and Twophase Flow in Porous Media: Approaches and Applications, Transp, vol. 130, Porous Media, 2019, pp. 77–104, https://doi.org/10.1007/s11242-019-01289-9.
- [17] Q. Xiong, T.G. Baychev, A.P. Jivkov, Review of pore network modelling of porous media: experimental characterisations, network constructions and applications to reactive transport, J. Contam. Hydrol. 192 (2016) 101–117, https://doi.org/ 10.1016/j.iconhyd.2016.07.002.
- [18] X. Feng, C.J. Burke, M. Zhuo, H. Guo, K. Yang, A. Reddy, I. Prasad, R.-M. Ho, A. Avgeropoulos, G.M. Grason, E.L. Thomas, Seeing mesoatomic distortions in softmatter crystals of a double-gyroid block copolymer, Nature 575 (2019) 175–179, https://doi.org/10.1038/s41586-019-1706-1.
- [19] W.A. Phillip, R. Mika Dorin, J. Werner, E.M.V. Hoek, U. Wiesner, M. Elimelech, Tuning structure and properties of graded triblock terpolymer-based mesoporous

- and hybrid films, Nano Lett. 11 (2011) 2892–2900, https://doi.org/10.1021/pl2013554
- [20] C.-Z. Qin, S. Hassanizadeh, L. Van Oosterhout, Pore-network modeling of water and vapor transport in the micro porous layer and gas diffusion layer of a polymer electrolyte fuel cell, Computation 4 (2016) 21, https://doi.org/10.3390/ computation4020021.
- [21] A. Raoof, S. Majid Hassanizadeh, A New Method for Generating Pore-Network Models of Porous Media, vol. 81, Porous Media, Transp, 2010, pp. 391–407, https://doi.org/10.1007/s11242-009-9412-3.
- [22] D. Ben-Avraham, A.F. Rozenfeld, R. Cohen, S. Havlin, Geographical embedding of scale-free networks, Phys. A Stat. Mech. Its Appl. (2003) 107–116, https://doi.org/ 10.1016/j.physa.2003.08.036.
- [23] H. Sai, K.W. Tan, K. Hur, E. Asenath-Smith, R. Hovden, Y. Jiang, M. Riccio, D. a Muller, V. Elser, L. a Estroff, S.M. Gruner, U. Wiesner, Hierarchical porous polymer scaffolds from block copolymers, Science 341 (80) (2013) 530–534, https://doi. org/10.1126/science.1238159
- [24] J. Yuan, E. Bae, X.-C. Tai, A study on continuous max-flow and min-cut approaches, in: 2010 IEEE Comput. Soc. Conf. Comput. Vis. Pattern Recognit., IEEE, 2010, pp. 2217–2224, https://doi.org/10.1109/CVPR.2010.5539903.
- [25] J. Yuan, C. Schörr, G. Steidl, Simultaneous higher-order optical flow estimation and decomposition, SIAM J. Sci. Comput. 29 (6) (2007) 2283–2304, https://doi. org/10.1137/060660709.
- [26] J. Yuan, E. Bae, X.-C. Tai, Y. Boykov, A Study on Continuous Max-Flow and Min-Cut Approaches, UCLA CAM, Technical Report 10-61, 2010. https://ww3.math.ucla.edu/camrenort/cam10-61.pdf.
- [27] Z. Niu, V.J. Pinfield, B. Wu, H. Wang, K. Jiao, D.Y.C. Leung, J. Xuan, Towards the digitalization of porous energy materials: evolution of digital approaches for microstructural design, Energy Environ. Sci. 14 (2021) 2549–2576, https://doi. org/10.1039/D1EE00398D.
- [28] R. Bostanabad, Y. Zhang, X. Li, T. Kearney, L.C. Brinson, D.W. Apley, W.K. Liu, W. Chen, Computational microstructure characterization and reconstruction: review of the state-of-the-art techniques, Prog. Mater. Sci. 95 (2018) 1–41, https://doi.org/10.1016/j.pmatsci.2018.01.005.

- [29] A. Rabbani, A.M. Fernando, R. Shams, A. Singh, P. Mostaghimi, M. Babaei, Review of data science trends and issues in porous media research with a focus on imagebased techniques, Water Resour. Res. 57 (2021) 1–44, https://doi.org/10.1029/ 2020WR029472
- [30] A. Mehmani, M. Prodanović, The effect of microporosity on transport properties in porous media, Adv. Water Resour. 63 (2014) 104–119, https://doi.org/10.1016/j. advwatres.2013.10.009.
- [31] B. Paisley, M.S. Riasi, L. Yeghiazarian, M.D. Grigoriu, Fast numerical design of porous materials with target permeability, porosity, and pore size distribution, J. Porous Media 24 (2021) 41–58, https://doi.org/10.1615/ JPprMedia 2020034996
- [32] I. Arganda-Carreras, R. Fernández-González, A. Muñoz-Barrutia, C. Ortiz-De-Solorzano, 3D reconstruction of histological sections: application to mammary gland tissue, Microsc. Res. Tech. 73 (2010) 1019–1029, https://doi.org/10.1002/jemt.20829.
- [33] G. Polder, H.L.E. Hovens, A.J. Zweers, A. Jahnen, C. Moll, A.J.F. Kennedy, Measuring shoot length of submerged aquatic plants using graph analysis, in: ImageJ User Dev. Conf., 2010, p. 7.
- [34] C.T. Rueden, J. Schindelin, M.C. Hiner, B.E. DeZonia, A.E. Walter, E.T. Arena, K. W. Eliceiri, ImageJ2: ImageJ for the next generation of scientific image data, BMC Bioinf. 18 (2017) 1–26, https://doi.org/10.1186/s12859-017-1934-z.
- [35] J. Schindelin, I. Arganda-Carreras, E. Frise, V. Kaynig, M. Longair, T. Pietzsch, S. Preibisch, C. Rueden, S. Saalfeld, B. Schmid, J.-Y. Tinevez, D.J. White, V. Hartenstein, K. Eliceiri, P. Tomancak, A. Cardona, Fiji: an open-source platform for biological-image analysis, Nat. Methods 9 (2012) 676–682, https://doi.org/ 10.1038/nmeth.2019.
- [36] C.A. Schneider, W.S. Rasband, K.W. Eliceiri, NIH Image to ImageJ: 25 years of image analysis, Nat. Methods 9 (2012) 671–675, https://doi.org/10.1038/ nmeth 2080
- [37] T. Sochi, The Flow of Newtonian Fluids in Axisymmetric Corrugated Tubes, 2010. ArXiv:1006.1515vol. 1, http://arxiv.org/abs/1006.1515.